Progress In Electromagnetics Research B, Vol. 61, 135–147, 2014

Imaging of 3-D Dielectric Objects Using Far-Field Holographic Microwave Imaging Technique

Lulu Wang[1, *], Ahmed M. Al-Jumaily[1], and Ray Simpkin[2]

Abstract—This paper describes the working principle of a three-dimensional (3-D) holographic microwave imaging (HMI) method for imaging small inclusion embedded in a dielectric object. Using published dielectric properties of various materials, a 3-D mathematical model is developed under the MATLAB environment to validate the HMI on various dielectric objects. Results indicate that the 3-D HMI has an ability to produce a 3-D image and detect small inclusions embedded within a dielectric object. Several potential applications of the 3-D HMI method includes biological tissues imaging, security screening and packaged food evaluation.

1. INTRODUCTION

There is a growing body of literature on the development of imaging methods for medical applications. Existing technologies are able to produce well-defined tomographic reconstructions of living tissues using various imaging approaches [1]. The most available imaging techniques include computed tomography (CT), magnetic resonance imaging (MRI), radiography (plain X-ray imaging), ultrasound (US), positron emission tomography (PET) and single photon emission computed tomography (SPECT). However, these techniques have some limitations [2], such as CT suffers from exposing the patient to doses of ionizing radiation, MRI is a very expensive technique, X-rays are less effective than both CT scanners and MRI, and the radiation is harmful to the human body. Overcome these limitations, microwave imaging has been proposed as a promising non-ionizing, non-invasive alternative screening technology.

Advantages of microwave imaging include microwave electronics and test instrumentation is mature, compact, and relatively cheaper compared to X-ray or MRI [3]. Microwaves and millimetre waves have been used extensively for imaging dielectric bodies [3]. The application of microwaves in biomedical imaging has gained growing attention among researchers in the past couple of decades with a particular focus on breast imaging [4]. Microwave imaging based techniques are appropriate for imaging human breasts due to the high contrast exists in the dielectric properties between malignant and healthy tissue [5]. Additional factors to support microwave breast imaging are that microwave signals attenuate significantly less (about 4 dB/cm for fat tissue at a frequency of 10 GHz) in healthy tissue, and breasts naturally protrude outside the human body.

Existing microwave imaging approaches can be classified into three large groups: ultra-wideband (UWB) radar techniques [6, 7], tomographic [7–12] and microwave holographic approaches [13–16]. Few clinical trials [17–20] have confirmed that microwave imaging is one of the most promising alternatives to X-ray mammography for early stage breast cancer detection. Microwave imaging based techniques have been extensively investigated for imaging of breast phantoms, some limitations including large reflections from skin, high cost of ultra-high speed digital electronics required for imaging in real-time, low-resolution image, not sensitive enough to small lesions, and large computation time required.

This paper demonstrates a new 3-D imaging algorithm based on our developed 2-D imaging method [21–28]. The 2-D HMI method was proposed based on holographic and aperture synthesis

Received 20 August 2014, Accepted 3 November 2014, Scheduled 5 November 2014

* Corresponding author: Lulu Wang (luwang@aut.ac.nz).

[1] Institute of Biomedical Technologies, AUT University, Auckland, New Zealand. [2] Callaghan Innovation, Auckland, New Zealand.

imaging techniques. Compared to most widely used Synthetic Aperture RADAR (SAR) technique, the microwave holographic based technique does not require expensive ultra-high speed electronics as narrow-band signals can be converted to the baseband for digitization at a slower rate [16]. A numerical model is developed to validate the proposed imaging method. Results demonstrated that the 3-D HMI imaging algorithm has an ability to produce 3-D images of breast-simulated dielectric objects and detect small lesions within the objects. Potential application of this technique would be internal organ imaging, such as breast, brain, and food evaluation. Potential advantages of this method include large inversion calculation is not required, low-cost and easy-to-use screening and diagnostic tool for imaging biological tissues.

2. 3-D HOLOGRAPHIC MICROWAVE IMAGING

Figure 1 displays a possible implementation of a 3-D HMI system. A dielectric object (not showing) is placed on the window of an examination bed. Referring to Figure 1(b), the proposed system consists of a single transmitter and 15 receivers. All antennas are surrounding within the antenna array plane, which are connected to a 16-channel switch. The antenna array plane is placed under the examination bed in the far-field region of the array ($> 6\lambda$) and it is designed to be moveable toward the target object in a vertical position. The space between the examination window and the antenna array plane is filled with host medium.

We assume that a point P is located within an object under test (Figure 2). Under far-field condition, the complex visibility function G of the back-scattered electric field, $\underline{E}_{scat}$, for any two receiving antennas located at $\underline{r_i}$ and $\underline{r_j}$ (see Figure 2) is defined as [29]:

$$G\left(\underline{r_i}, \underline{r_j}\right) = \left\langle \underline{E}_{scat}\left(\underline{r_i}\right) \cdot \underline{E}^*_{scat}\left(\underline{r_j}\right) \right\rangle \tag{1}$$

where $\langle\,\rangle$ represents the expectation value (time average). See Table 1 for definitions of symbols used in Equation (1) and elsewhere in this paper.

Referring to [22], the intensity distribution of the object $I(\underline{s})$ at position $\underline{s}$ is defined as:

$$I\left(\underline{s}\right) = \left(\frac{k_0^2}{4\pi}\right)^2 \left|\varepsilon\left(\underline{s}\right) - \varepsilon_1\right|^2 \underline{E}_{tot}(\underline{s}) \cdot \underline{E}^*_{tot}\left(\underline{s}'\right) \tag{2}$$

The quantity that we reconstruct at each voxel is that defined in (2), which we simply refer to as 'intensity'. Physically, this quantity is proportional to the squared modulus of the polarisation charge

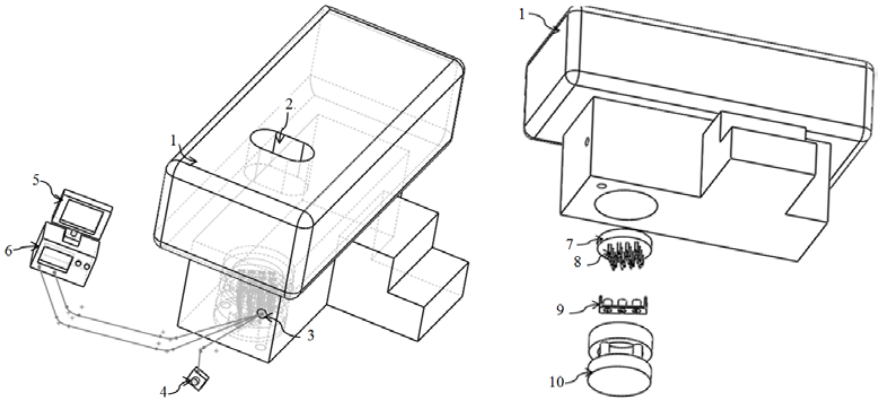

Figure 1. (a) 3-D holographic microwave imaging system, (b) bottom view of examination bed (1: examination bed, 2: examination window, 3: connection hole to antennas, 4: multi-position switch, 5: computer, 6: microwave generator, 7: antenna array plane, 8: antennas, 9: multi-position switch assembly, 10: antenna array holder).

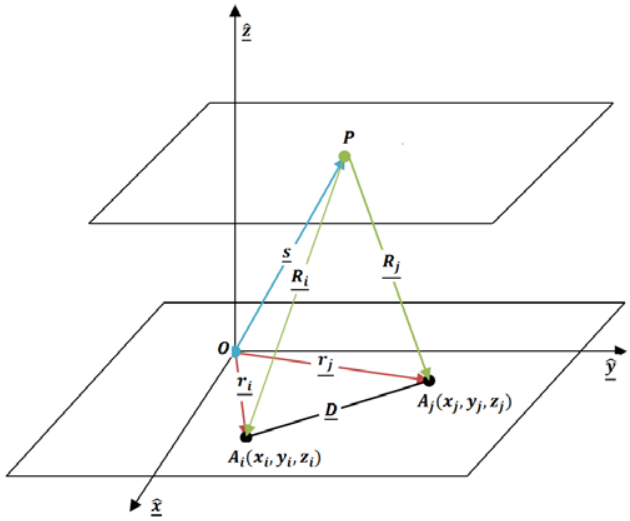

Figure 2. Geometry of HMI measurement by a pair of receivers.

Table 1. Symbol definitions.

k_0	Free-space propagation
k_1	Wavenumber of host medium
$\varepsilon(\underline{s})$	Complex relative permittivity distribution inside the dielectric object
ε_1	Relative permittivity of the host medium
$\underline{E}_{tot}(\underline{s})$	Total electric field at a point inside the object with position vector, $\underline{s}$
$\underline{E}_0$	Wave amplitude of TE_{10} mode at within waveguide aperture
λ_1	Wavelength in the host medium
$\widehat{\underline{R}}$	Unit vector parallel to the vector $\underline{R}$
R	Distance from a point in the object to the receiver
$\underline{R}$	Position vector from a point in the object to the selected receiver
R_0	Distance from a point in the object to the transmitter
A	Narrow aperture dimension of antenna aperture
B	Broad aperture dimension of antenna aperture
$h(\theta, \emptyset)$	radiation pattern function
$\underline{P}(\theta, \emptyset)$	polarization vector

density at each point inside the object. Note that this is a scalar quantity, which simplifies the image reconstruction.

The baseline vector $\underline{D}$ of any two receivers (see Figure 2) can be written in Cartesian components as below:

$$u = \left(\underline{x_j} - \underline{x_i}\right)/\lambda_1; \quad v = \left(\underline{y_j} - \underline{y_i}\right)/\lambda_1; \quad w = \left(\underline{z_j} - \underline{z_i}\right)/\lambda_1 \tag{3}$$

As all antennas are located on a flat plane (2-D), a line integral along the radial coordinate, s, is defined [21]:

$$\tilde{I}(l, m) = \int_s \frac{I(s, l, m)}{\sqrt{1 - l^2 - m^2}} ds \tag{4}$$

where variables (l, m) are (referring to Figure 3) $l = \sin\theta\cos\phi$ and $m = \sin\theta\sin\phi$.

The 2-D intensity function of the object under test is given [21]:

$$\tilde{I}(l, m) = \iint G(u, v, w = 0)\, e^{j2\pi(ul+vm)} dl dm \tag{5}$$

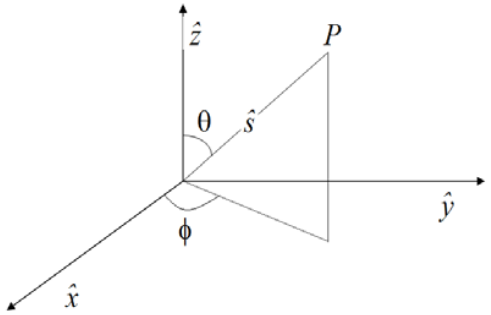

Figure 3. Spherical polar coordinate system.

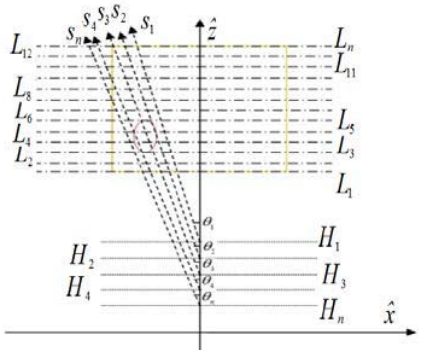

Figure 4. Block diagram showing the scattering characterization scheme from different receiving height H_n.

Equation (4) shows that a 2-D image can be determined by Fourier inversion and it is a projection of the 3-D intensity function onto a 2-D plane in $(l,\, m)$ space.

The antenna array plane is designed to be movable along the z-axis from H_1 to H_n in M equal steps, where H is the vertical distance between the antenna array plane and the target object (see Figure 4). A target point at the object depth location, z_n, within the same object is defined as:

$$z_n = s_n \left(\cos \theta_n\right) \tag{6}$$

where θ_n is the antenna receiving angle of the position s_n with the antenna array plane placed at the selected height H_n. Thus ds in Equation (4) becomes:

$$ds = \frac{dz}{\cos\left(\theta_n\right)} = \frac{dz}{\sqrt{1 - l^2 - m^2}} \tag{7}$$

Differentiating the intensity function with respect to s, then 3-D intensity function of the object at a selected height is given:

$$I\left(H = z_n, l, m\right) = d\tilde{I}(l, m) \cdot \left(1 - l^2 - m^2\right) / dz \tag{8}$$

The derivative in Equation (8) can be approximated by the following forward difference expression:

$$\frac{d\tilde{I}}{dz} = \frac{\tilde{I}_{Z_n} - \tilde{I}_{Z_{n-1}}}{Z_n - Z_{n-1}} \tag{9}$$

The complex visibility function is computed using Equation (1) for all possible pairs of receiving antennas, with the background scattered field subtracted from the data. For example, for N receivers, the measured complex visibility data is $N(N-1)$.

Referring to Equations (1) and (5), a 2-D image can be represented using complex visibility data that is collected when the antenna array plane is placed at the selected height. The development of 2-D image algorithm is documented in [21]. A reconstructed 3-D image of the object is then computed using (8) and (9) by acquiring measured data with the antenna array placed at different heights, and computing the sequence of 2-D images $\tilde{I}_{Z_n}$. The remainder of this paper describes computer simulations related to 3-D images.

3. SIMULATION

3.1. System Configuration

Previously published experimental work of 2-D holographic microwave imaging technique demonstrated that reasonable resolution of 2-D images can be obtained using data acquired at just one frequency [25, 26]. Although only a single frequency of 12.6 Hz was selected for reconstructing the

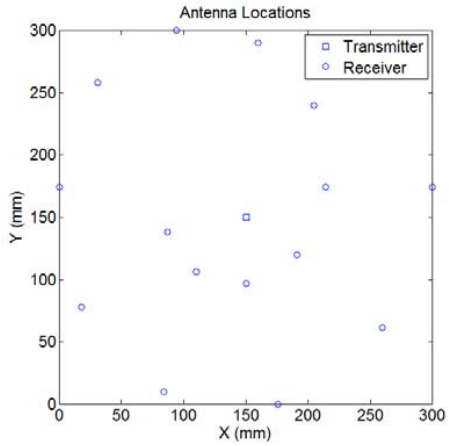

Figure 5. Antenna array configuration.

image, data was recorded at 3201 frequency points for choosing the optimum frequency between 10 GHz to 20 GHz and 101 measurements were averaged at each frequency [25, 26]. The 2-D HMI technique was developed based on aperture synthesis imaging technique that is similar to the one widely used in radio astronomy, therefore antenna array configuration plays an important role in producing a high resolute image. Optimization of antenna numbers, antenna array configurations, and the distance between the antenna array plane and the target object to produce high-resolution image are detailed in [27, 28].

Based on achieved simulation and experimental results of 2-D HMI technique [25–27], a computer model was developed to validate the 3-D HMI technique. One possible implementation of HMI system is presented in Figure 1. The examination bed contains a window that made of material with lossless dielectric material, and the object under test was placed in the window. A 16-element antenna array plane (see Figure 5) was placed and moved from $z = -460\,\text{mm}$ (19.3λ) to $z = -440\,\text{mm}$ (18.5λ) in 20 equal steps (0.04λ). The target object was located at $z = 0\,\text{mm}$ and was assumed to be fully contained in a rectangle imaging domain with length 150 mm (6.3λ). The space between the antenna array plane and the examination widow was filled with dielectric material (same as examination window material).

3.2. Waveguide Antenna and Scattered Field

A small open-ended rectangular waveguide was assumed as both transmitter and receivers. The radiated far-field, $\underline{E}_{inc}$, from such antenna is well-represented as:

$$\underline{E}_{inc}(R,\theta,\emptyset) = \left(-\frac{jk_1}{2\pi^2}\right)\underline{E}_0\left(\frac{e^{-jk_1R_0}}{R_0}\right)ABh(\theta,\emptyset)\,\underline{P}(\theta,\emptyset) \tag{10}$$

It is well-known that the back-scattered field can be represented as an integral over the volume of the scatterer involving the induced polarization currents that arise from the complex permittivity contrast within the free space. The scattered field at any receiver can be found by applying the Stratton & Chu formulation [30]:

$$\underline{E}_{scat} = \frac{k_0^2}{4\pi}\int\limits_V (\varepsilon(\underline{s}) - \varepsilon_1)\left\{a\underline{E}_{tot}(\underline{s}) + \left(b\underline{E}_{tot}(\underline{s})\cdot\widehat{\underline{R}}\right)\widehat{\underline{R}}\right\}\frac{e^{-jk_1R}}{R}dV \tag{11}$$

where $a = 1 - j/k_1R - 1/(k_1R)^2$; $b = -1 + 3j/k_1R + 3/(k_1R)^2$.

When $k_1R \gg 1$, the above factors can be approximated by $a \approx 1$ and $b \approx -1$.

We used both Method of Moments (MoM) and Born Approximation methods to evaluate the 2-D HMI technique [22, 23]. For the purposes of demonstrating the HMI technique, it is computationally advantageous to consider a small permittivity contrast between the target and host medium thus $(\varepsilon(\underline{s}) - \varepsilon_1)$ is assumed to be small. In this case, the back-scattered field can be readily determined

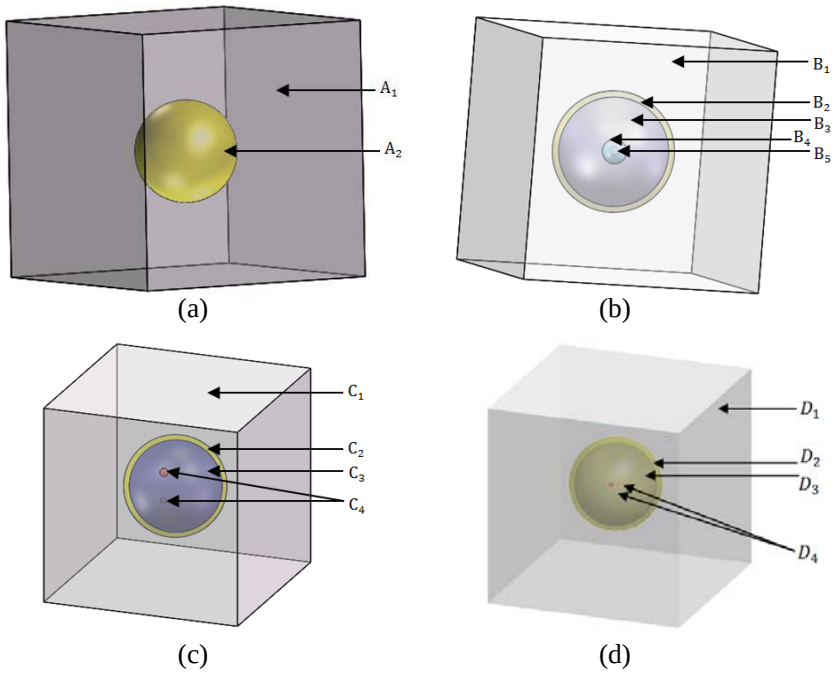

Figure 6. Models under test. (a) Model I. (b) Multimedia dielectric object II. (c) Multimedia dielectric object III. (d) Multimedia dielectric object IV within loss matching medium (A_1: background cube, A_2: skin, B_1 is background cube, B_2: breast skin, B_3: breast fat, B_4: breast gland, B_5: breast lesion, C_1: background cube, C_2: breast skin, C_3: breast fat, C_4: breast lesion, D_1: background cube, D_2: skin, D_3: fat, D_4: lesion).

Table 2. Models under test.

Model	No.	Material	Shape	Thickness (mm)	Location (mm)			Dielectric properties [31]		Scale value of dielectric properties	
					x	y	z	ε_r	σ (s/m)	ε_r	σ (s/m)
I	A_1	Medium	Cube	150	75	75	75	36	0	36	0
	A_2	skin	Spherical	60	75	75	75	36	4	36	4
II	B_1	Medium	Cube	100	50	50	50	9	0	0.18	0
	B_2	Skin	Spherical	5	50	50	50	36	4	0.72	0.4
	B_3	Fat	Spherical	45	50	50	50	9	0.4	0.18	0.04
	B_4	Gland	Spherical	10	50	50	50	13	0.45	0.26	0.045
	B_5	Lesion	Spherical	4	50	50	50	50	0.4	1	0.04
III	C_1	Medium	Cube	100	50	50	50	9	0	0.18	0
	C_2	Skin	Spherical	5	50	50	50	36	4	0.72	0.4
	C_3	Fat	Spherical	45	50	50	50	9	0.4	0.18	0.04
	C_4	Lesion 1	Spherical	4	30	50	60	50	0.4	1	0.04
	C_4	Lesion 2	Spherical	3	30	50	30	50	0.4	1	0.04
IV	D_1	Medium	Cube	110	55	55	55	36	2	0.72	0.2
	D_2	Skin	Spherical	5	55	55	55	36	4	0.72	0.4
	D_3	Fat	Spherical	45	55	55	55	9	0.4	0.18	0.04
	D_4	Lesion 1	Spherical	3	55	55	55	50	6	1	0.6
	D_4	Lesion 2	Spherical	3	48	48	55	50	6	1	0.6

using the Born Approximation, which allows the total electric field $\underline{E}_{tot}$ to be approximated by the incident field, so that we obtain:

$$\underline{E}_{scat}(\underline{r}) = \left(\frac{k_0^2}{4\pi}\right) \int_V (\varepsilon(\underline{s}) - \varepsilon_1) \left\{ \underline{E}_{inc}(\underline{s}) + \left(\underline{E}_{inc}(\underline{s}) \cdot \widehat{\underline{R}}\right) \hat{\underline{R}} \right\} \frac{e^{-jk_1 R}}{R} dV \tag{12}$$

Assume $\underline{E}_{inc}(\underline{s}) \cdot \hat{\underline{R}} \approx 0$ referring to far-field condition, and then the back-scattered field can be obtained:

$$\underline{E}_{scat}(\underline{r}) = \left(\frac{k_0^2}{4\pi}\right) \int_V (\varepsilon(\underline{s}) - \varepsilon_1) \underline{E}_{inc}(\underline{s}) \frac{e^{-jk_1 R}}{R} dV \tag{13}$$

3.3. Target Object

To create 3-D images using the 3-D HMI technique, several dielectric objects including single and multiple small inclusions were considered. Four models are presented in this paper (see Figure 6). Table 2 summaries the material, shape, size, and dielectric properties of models under test.

Figure 6(a) shows a schematic drawing of model I, where the single media dielectric object is placed at the centre of a cube background. The target object has the dielectric properties of the human skin. The cube was made of lossless dielectric material ($\varepsilon_r = 36$) and it was placed at the window of

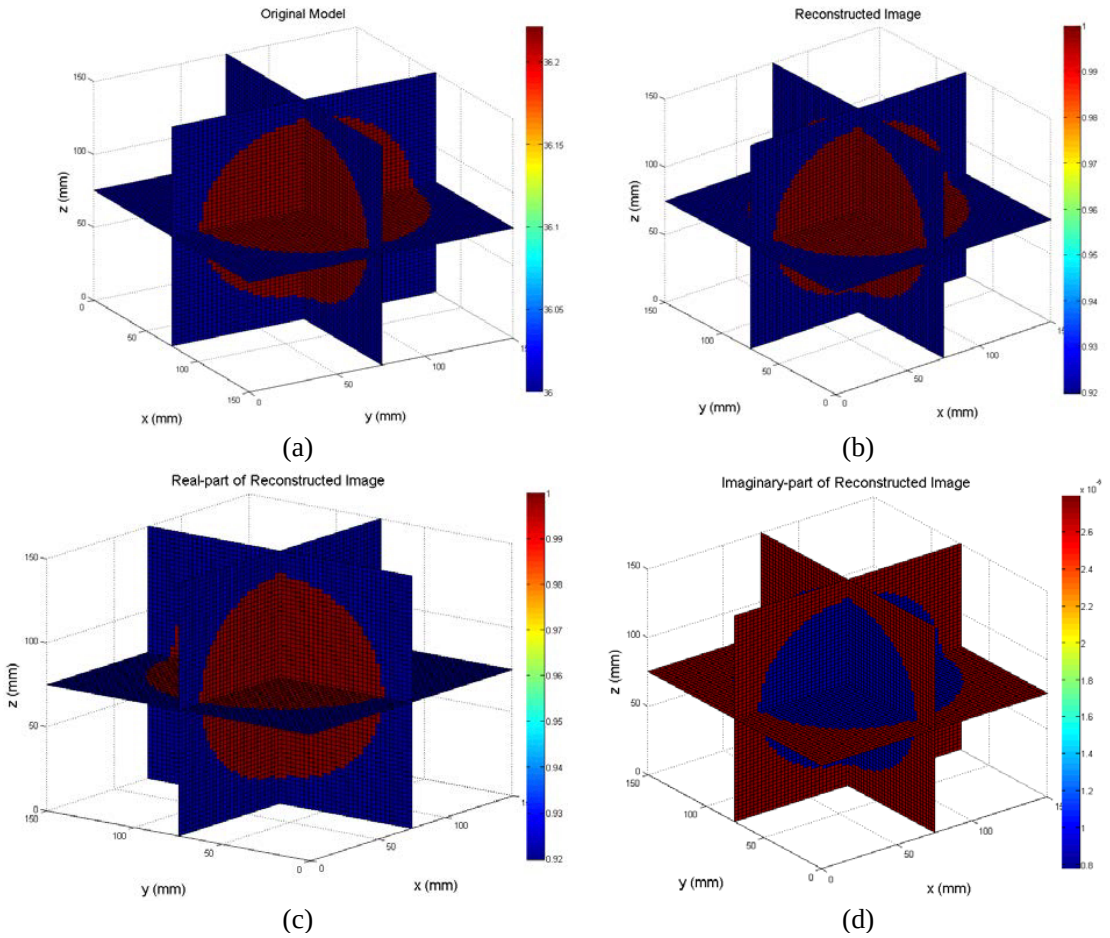

Figure 7. (a) Original image of object I (modulus-part). (b) 3-D reconstructed image of object I (modulus-part). (c) Reconstructed amplitude image. (d) Reconstructed phase image.

examination bed. The space between the window and the antenna array plane was filled with a lossless dielectric material ($\varepsilon_r = 36$).

Figure 6(b) displays a schematic drawing of model II, where the multimedia dielectric object II is placed at the centre of the cube. This multimedia object II was assumed as a breast that contains breast skin, fat, gland and one lesion. The scale values of the published dielectric properties of real breast tissues were applied to assume a small permittivity contrast between the object and the host medium as detailed in Section 4.2.

Figure 6(c) shows a simulated model III, which is placed at the centre of the cube. We assumed the object III as a breast that contains breast skin, fat, and two lesions. The distance between the two lesions was 1.27λ. The location, size and dielectric properties of the model III are detailed in Table 2.

Figure 6(d) presents a simulated model IV, which is placed at the centre of the cube (loss dielectric material). We assumed object IV as a breast that contains breast skin, fat, and two lesions. The location, size and dielectric properties of the model IV are detailed in Table 2.

A 3-D computer model was developed using MATLAB software by combining (1) and (13) to compute the complex visibility function. 3-D images of the object under test governed by Equations (8) and (9).

4. IMAGING RESULTS

During operation, one port of a microwave generator excites electromagnetic waves to the single transmitting antenna at single frequency of 12.6 GHz ($\lambda = 23.8$ mm). The magnitude and phase of

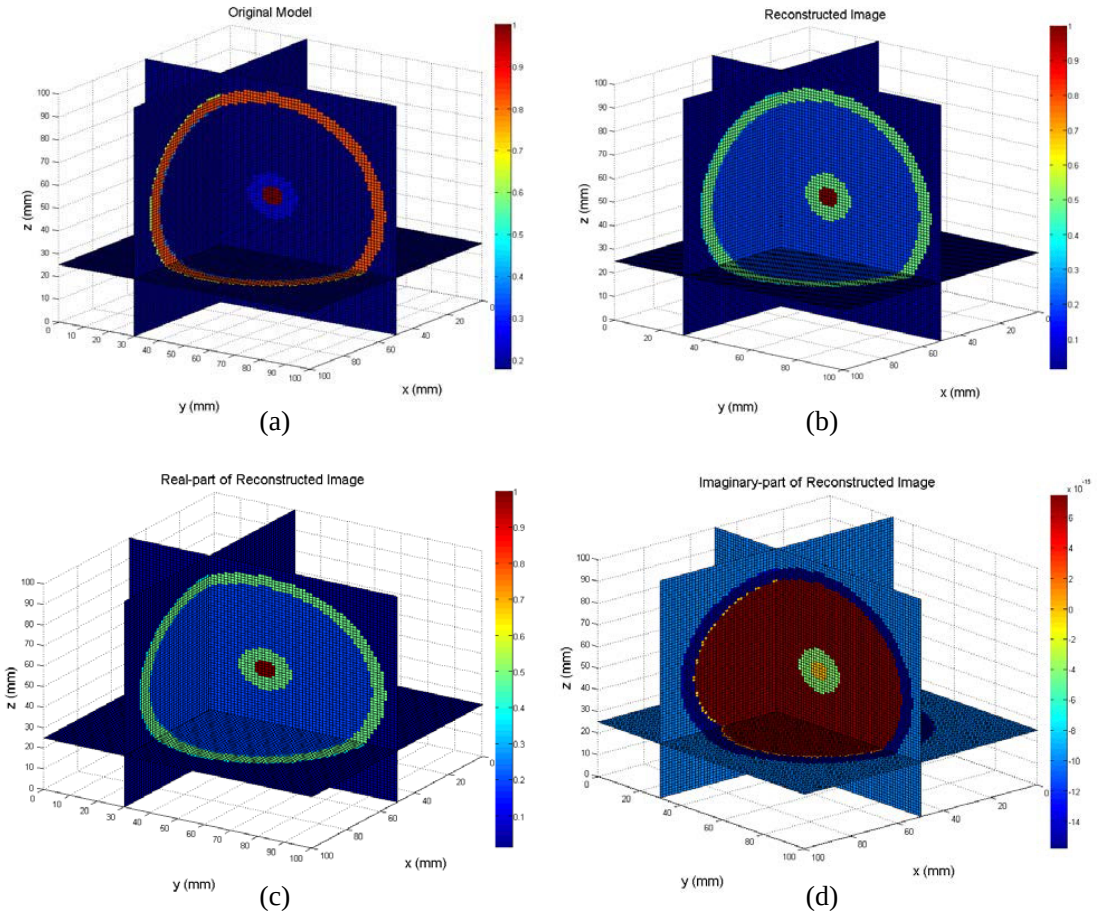

Figure 8. (a) Original image of object II (modulus value). (b) 3-D reconstructed image of object II (modulus-part). (c) Reconstructed amplitude image. (d) Reconstructed phase image.

the back-scattered electric field from the target object was recorded at each receiver element on the array plane, which was connected to the second port of the microwave generator via a multi-position switch. The simulated back-scattered field (phase and magnitude) from the object then was applied to mapping the energy density of the object to produce a 2-D image. These steps were repeated for every new vertical position of the antenna array and a 3-D image of the object was created by combing a sequence of 2-D images when antenna array plane placed at different vertical positions.

Figure 7(a) shows the original image of model I. The cube image region (150 mm×150 mm×150 mm) containing the target object (Skin) and the background medium (lossless material close to skin) is uniformly subdivided into 60 × 60 × 60 elementary square cells. The modulus-part, real-part and imaginary-part of reconstructed images of model I are presented in Figures 7(b), (c), and (d). The simulation time was approximately 3.5 minutes for model I.

Figure 8 displays the original image and 3-D reconstructed images of model II. Model II contains a breast that is made of skin (5 mm thinness), fat, gland (10 mm in diameter), and one lesion (4 mm in diameter), where the breast model was located on the examination bed at $z = 0$ mm and the antenna array plane was placed at $z = -460$ mm and moved to $z = -440$ mm in 20 steps during screening. The cube image region (100 mm × 100 mm × 100 mm) containing the target object (breast) and the background medium (lossless material close to fat tissue) is uniformly subdivided into 80 × 80 × 80 elementary square cells. The total simulation time for Model II was approximately 10 minutes.

Figure 9(a) illustrates the original 3-D image of the model III containing a breast and background cube (lossless material close to fat tissue). The breast contains skin (5 mm thinness), fat, and two lesions (3 and 4 mm in diameter respectively). The image region (100 mm × 100 mm × 100 mm) is uniformly subdivided into 85 × 85 × 85 elementary square cells. Two lesions were located in ($x_1 = 30$, $y_1 = 50$,

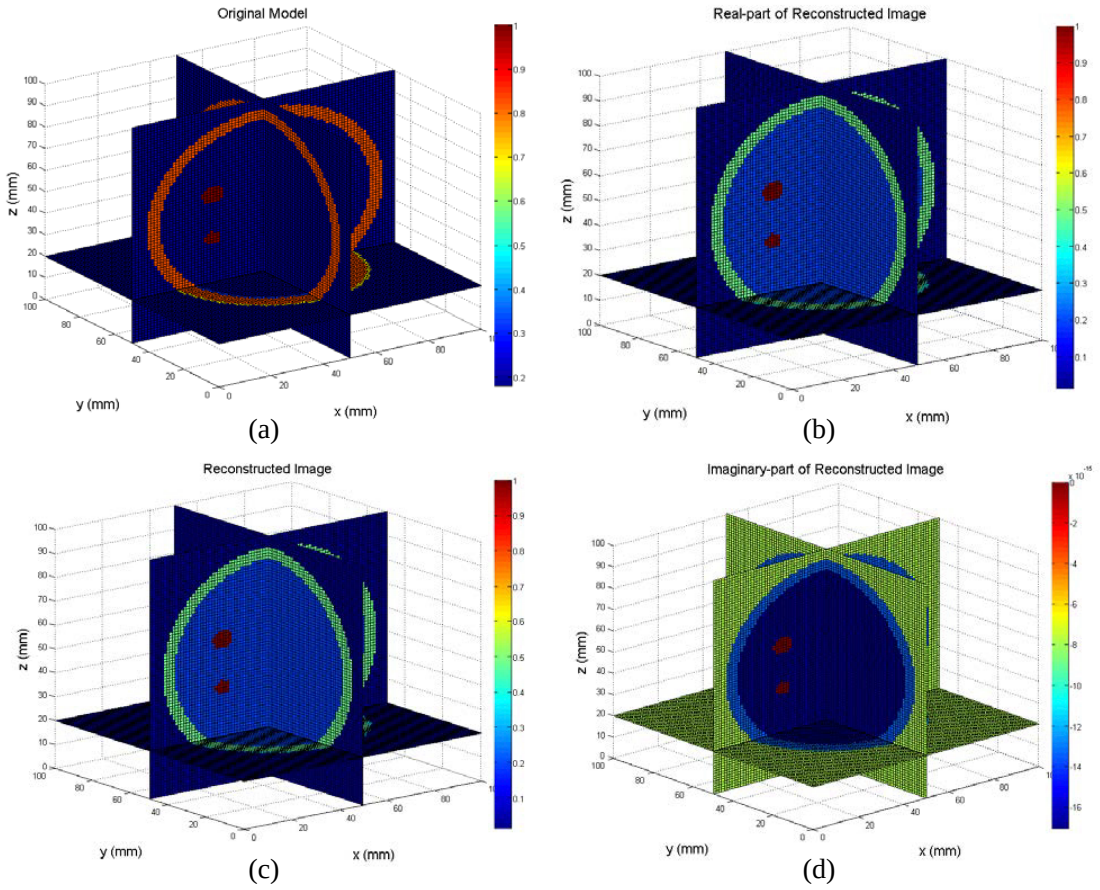

Figure 9. (a) Original image of object III (modulus-part). (b) 3-D reconstructed image of object III (modulus-part). (c) Reconstructed amplitude image. (d) Reconstructed phase image.

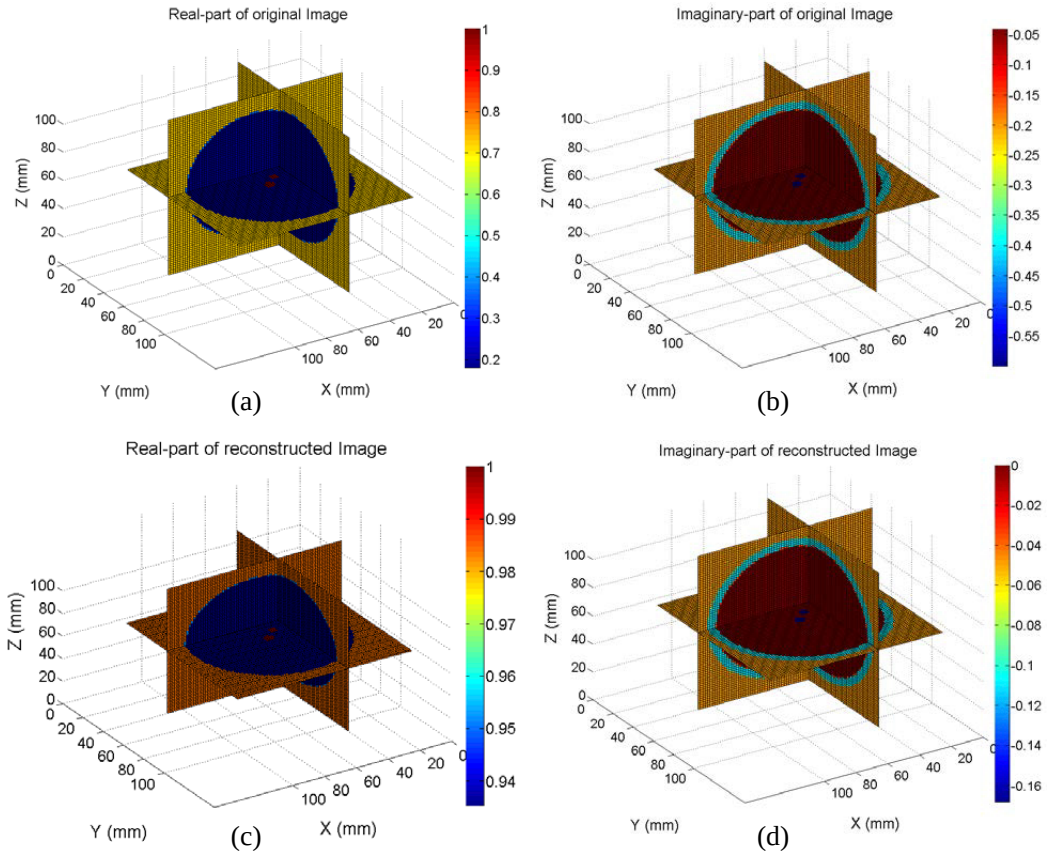

Figure 10. (a) Original image of object IV (real-part). (b) Original image of object IV imaginary-part). (c) 3-D 260 reconstructed image of object IV (real-part). (d) 3-D reconstructed image of object IV (imaginary-part).

$z_1 = 60$) and ($x_2 = 30$, $y_2 = 50$, $z_1 = 30$), respectively. Reconstructed images of model III are presented in Figure 9(b), Figure 9(c) and Figure 9(d). The total simulation time for model III was approximately 14.5 minutes.

Figure 10(a) and Figure 10(b) present the real-part and imaginary-part of model IV containing a breast and background cube (loss material close to the skin). The breast contains skin (5 mm thinness), fat, and two lesions (3 in diameter). The image region (110 mm × 110 mm × 110 mm) is uniformly subdivided into 74 × 74 × 74 elementary square cells. Two lesions were located in ($x_1 = 55$, $y_1 = 55$, $z_1 = 55$) and ($x_2 = 48$, $y_2 = 48$, $z_1 = 55$), respectively. Reconstructed images of model IV are presented in Figure 9(c) and Figure 9(d). The total simulation time for model IV was approximately 7 minutes.

Results show that all dielectric objects are successfully imaged and structures of objects are clearly identified. Small inclusions (lesion) within a multimedia dielectric object (breast) also fully imaged using the 3-D HMI technique. Colour bars in Figure 7(a), Figure 8(a) and Figure 9(a) plot the dielectric properties (modulus value) of objects. Colour bars in Figure 10(a) and Figure 10(b) plot permittivity and conductivity values of the object, respectively. In reconstructed images, colour bars plot signal energy on a linear scale, normalised to the maximum in the 3-D image space and values below 0.1 are rendered as blue.

5. DISCUSSION AND CONCLUSIONS

This paper reports the development of the 3-D HMI method for imaging of dielectric objects and theoretical validation of the technique using various dielectric objects. This new method uses physical displacement between the antenna array plane and the imaged object over a specified range (vertical)

to obtain depth information from sequence 2-D images. The contrast between breast lesion, fat tissue, gland and skin is very close to the real breast.

The image quality depends highly on the antenna baseline difference, in other words, the antenna locations on a 2-D array plane as presented in Equation (3). The presented antenna array in this paper provides the maximum combination of receiving antennas and enables the collection of out of plane transmission data [24, 25]. Optimization of antenna array configurations to generate high resolute images is detailed in [27]. Pervious work [28] demonstrated that in real measurement environmental, the scale product of 2-D image $\tilde{I}_{Z_n}$ and antenna array configuration are helpful to reduce measurement noise.

The major limitation of the developed 2-D imaging method is that only one object can be imaged if more than one object located at the same x and y coordinates but at different z-planes. Numerical results presented in this work demonstrate that multiple small inclusions (lesions) located at different locations within the object (breast) could be fully detected, which proves that the 3-D imaging algorithm has an ability to solve the limitation of the 2-D imaging technique. The major limitation of the 3-D HMI numerical model is a large amount of high-speed memory required for quality 3-D images, which increases the simulation time and operation cost.

Compared to other microwave imaging systems, the most significant benefit of the proposed technique is that we can obtain 3-D images of reasonable resolution using data acquired at just one frequency. We do not need to use broadband systems and measurements like UWB radar methods. A matching medium was not required in this preliminary 2-D HMI measurement system [22–25], only air, which greatly simplified the practical implementation of such a system and reduced the associated cost. However, this claim needs further substantiation when the system is used with real biological tissues.

Implementation of the proposed 3-D HMI technique on realistic biological tissue phantoms and real biological tissues as well as human tissues is currently an undergoing project, and results are planned to be reported in the future. The 3-D HMI technique has wide potential applications, such as imaging of biological tissues, security screening or packaged food evaluation. An important issue that will need to be addressed in the future is the extension of the analysis to 3-D tissue models with realistic shape and realistic tissue architecture. In the case of breast cancer detection using the 3-D HMI technique, further areas of study include:

- Development of a realistic breast phantom that is close to real human tissue architecture.
- Design and build a compact patch antenna array suitable for a clinical trail system set-up.
- Validation of the 3-D HMI technique through measurement studies on realistic breast phantoms.
- Validation of the 3-D HMI technique through measurement studies on living tissues and mastectomy tissue.
- Comparison between HMI technique and other microwave imaging approaches, as well as existing medical imaging tools such as X-ray mammography and MRI.

REFERENCES

1. Ghavami, N., G. Tiberi, D. J. Edwards, and A. Monorchio, "UWB microwave imaging of objects with canonical shape," *IEEE Transactions on Antennas and Propagation*, Vol. 60, No. 1, 231–239, 2012.
2. Irishina, N., "Microwave medical imaging using level set techniques," Ph.D. Dissertation, Charles III University of Madrid, Spain, 2009.
3. Nikolova, N. K., "Microwave imaging for breast cancer," *IEEE Microwave Magazine*, Vol. 12, No. 7, 78–94, 2011.
4. Hassan, A. M. and E. Shenawee, "Review of electromagnetic techniques for breast cancer detection," *IEEE Reviews in Biomedical Engineering*, Vol. 4, 103–118, 2011.
5. Zhu, G. K., "Application of microwave techniques in breast imaging," Ph.D. Thesis, McGill University, Montreal, Canada, 2011.

6. Klemm, M., I. J. Craddock, J. A. Leendertz, A. Preece, and R. Benjamin, "Radar-based breast cancer detection using a hemispherical antenna array — Experimental results," *IEEE Transactions on Antennas and Propagation*, Vol. 57, No. 6, 1692–1704, 2009.
7. Klemm, M., J. Leendertz, D. Gibbins, I. J. Craddock, A. Preece, and R. Benjamin, "Microwave radar-based differential breast cancer imaging: Imaging in homogeneous breast phantoms and low contrast scenarios," *IEEE Transactions on Antennas and Propagation*, Vol. 58, No. 7, 2337–2344, 2010.
8. Fang, Q., P. M. Meaney, S. D. Geimer, A. V. Streltsov, and K. D. Paulsen, "Microwave image reconstruction from 3-D fields coupled to 2-D parameter estimation," *IEEE Trans. on Medical Imaging*, Vol. 23, No. 4, 475–484, 2004.
9. Rubæk, T., O. S. Kim, and P. Meincke, "Computational validation of a 3-D microwave imaging system for breast-cancer screening," *IEEE Transactions on Antennas and Propagation*, Vol. 57, No. 7, 2105–2115, 2009.
10. Fear, E. C., "Microwave imaging of the breast," *Technology in Cancer Research & Treatment*, Vol. 4, No. 1, 69–82, 2005.
11. Tipa, R. and O. Baltag, "Microwave thermography for cancer detection," *Romanian Journal of Physics*, Vol. 51, Nos. 3–4, 371, 2006.
12. Grzegorczyk, T. M., P. M. Meaney, P. A. Kaufman, R. M. di Florio-Alexander, and K. D. Paulsen, "Fast 3-D tomographic microwave imaging for breast cancer detection," *IEEE Trans. on Medical Imaging*, Vol. 31, No. 8, 1584–1592, 2012.
13. Smith, D., M. Leach, M. Elsdon, and S. J. Foti, "Indirect holographic techniques for determining antenna radiation characteristics and imaging aperture fields," *IEEE Antennas and Propagation Magazine*, Vol. 49, No. 1, 54–67, 2007.
14. Ravan, M., R. K. Amineh, and N. K. Nikolova, "Two-dimensional near-field microwave holography," *Inverse Problems*, Vol. 26, No. 5, 055011, 2010.
15. Amineh, R. K., M. Ravan, A. Khalatpour, and N. K. Nikolova, "Three-dimensional near-field microwave holography using reflected and transmitted signals," *IEEE Transactions on Antennas and Propagation*, Vol. 59, No. 12, 4777–4789, 2011.
16. Jayanthy, M., N. Selvanathan, M. Abu-Bakar, D. Smith, H. M. Elgabroun, P. M. Yeong, and S. S. Kumar, "Microwave holographic imaging technique for tumour detection," *3rd Kuala Lumpur International Conference on Biomedical Engineering*, 275–277, 2006.
17. Meaney, P. M., M. W. Fanning, T. Raynolds, C. J. Fox, Q. Fang, C. A. Kogel, and K. D. Paulsen, "Initial clinical experience with microwave breast imaging in women with normal mammography," *Academic Radiology*, Vol. 14, No. 2, 207–218, 2007.
18. Halter, R. J., T. Zhou, P. M. Meaney, A. Hartov, R. J. Barth, Jr., K. M. Rosenkranz, and K. D. Paulsen, "The correlation of in vivo and ex vivo tissue dielectric properties to validate electromagnetic breast imaging: Initial clinical experience," *Physiological Measurement*, Vol. 30, No. 6, S121, 2009.
19. Meaney, P. M., P. A. Kaufman, L. S. Muffly, M. Click, S. P. Poplack, W. A. Wells, and K. D. Paulsen, "Microwave imaging for neoadjuvant chemotherapy monitoring: Initial clinical experience," *Breast Cancer Res.*, Vol. 15, No. 2, 1–16, 2013.
20. Fear, E. C., J. Bourqui, C. Curtis, D. Mew, B. Docktor, and C. Romano, "Microwave breast imaging with a monostatic radar-based system: A study of application to patients," *IEEE Trans. on Microwave Theory and Techniques*, Vol. 61, No. 5, 2119–2128, 2013.
21. Wang, L., R. Simpkin, and A. M. Al-Jumaily, "Holographic microwave imaging array for early breast cancer detection," *ASME 2012 International Mechanical Engineering Congress and Exposition*, 45–51, American Society of Mechanical Engineers, 2012.
22. Wang, L., A. M. Al-Jumaily, and R. Simpkin, "Holographic microwave imaging array for brain stroke detection," *Journal of Signal and Information Processing*, Vol. 4, No. 3B, 96–101, 2013.
23. Wang, L., R. Simpkin, and A. M. Al-Jumaily, "Holographic microwave imaging for medical applications," *Journal of Biomedical Science and Engineering*, Vol. 6, 823–833, 2013.

24. Wang, L., R. Simpkin, and A. M. Al-Jumaily, "3D breast cancer imaging using holographic microwave interferometry," *Proceedings of the 27th Conference on Image and Vision Computing*, 180–185, ACM, New Zealand, 2012.
25. Wang, L., R. Simpkin, and A. M. Al-Jumaily, "Holographic microwave imaging array: Experimental investigation of breast tumour detection," *2013 IEEE International Workshop on Electromagnetics (iWEM)*, 61–64, 2013.
26. Wang, L., R. Simpkin, and A. M. Al-Jumaily, "Open-ended waveguide antenna for microwave breast cancer detection," *2013 IEEE International Workshop on Electromagnetics (iWEM)*, 65–68, 2013.
27. Wang, L., A. M. Al-Jumaily, and R. Simpkin, "Antenna array configuration in holographic microwave imaging," *2014 ASME International Mechanical Engineering Congress & Exposition*, Paper No. IMECE2014-36556, Montreal, Canada, Nov. 14–20, 2014.
28. Wang, L., "Holographic microwave imaging for lesion detection," Doctoral Dissertation, Auckland University of Technology, 2013.
29. Levanda, R. and A.Leshem, "Synthetic aperture radio telescopes," *IEEE Signal Processing Magazine*, Vol. 27, No. 1, 14–29, 2010.
30. Silver, S., "Radiation from current distributions," *Microwave Antenna Theory and Design*, 87–90, S. Peter Peregrinus Ltd., London, UK, 1984.
31. Lazebnik, M., D. Popovic, L. McCartney, C. B. Watkins, M. J. Lindstrom, J. Harter, and S. C. Hagness, "A large-scale study of the ultrawideband microwave dielectric properties of normal, benign and malignant breast tissues obtained from cancer surgeries," *Physics in Medicine and Biology*, Vol. 52, No. 20, 6093, 2007.